Narrow and intense resonances in the low-frequency region of surface-enhanced Raman spectra of single-wall carbon nanotubes

Alexander A. Puretzky, David B. Geohegan, and Christopher M. Rouleau
Oak Ridge National Laboratory, Oak Ridge, Tennessee 37831-6488, USA
(Received 24 August 2010; published 2 December 2010)

Previously unexplored low-frequency Raman modes of single-wall carbon nanotubes (SWNTs) are reported. Gold deposited onto a randomly-oriented top layer of vertically aligned carbon nanotube arrays was used to induce surface-enhanced Raman scattering (SERS) "hot spots" on large-diameter SWNTs with SERS intensities up to 1900 times greater than normal Raman intensities from undecorated arrays. The linewidths of the resonances (down to 0.3 cm^{-1}) are ten times narrower than previously measured for individual SWNTs. Pairs of intense sharp resonances with identical excitation profiles were found and tentatively interpreted as the low-energy longitudinal optical and radial breathing modes of the same nanotube. SERS lines in the region of 14–30 cm^{-1} were tentatively assigned to the ring modes of SWNTs in agreement with existing theories.

DOI: 10.1103/PhysRevB.82.245402 PACS number(s): 78.67.Ch, 73.22.−f, 78.30.Na, 78.55.−m

I. INTRODUCTION

Resonance Raman spectroscopy of single-wall carbon nanotubes (SWNTs) has provided the most valuable information for basic theories of one-dimensional (1D) systems and has emerged into one of the most common characterization tools for SWNTs, their composites, and derivatives.[1–3] The most important information has been derived from numerous experimental investigations of the low-frequency radial breathing mode (RBM) of SWNTs, resulting in such significant theoretical refinements that unambiguous assignment of SWNT structure,[4–15] understanding of excitonic effects,[16] and assessment of environmental effects on Raman spectra[9] have been enabled. Most of these studies have been conducted for vibrational frequencies above ~100 cm^{-1}, corresponding to nanotube diameters smaller than ~2.5 nm.

Room-temperature linewidths for RBMs have been predicted to minimize at ~3 cm^{-1} for relatively small diameter SWNTs and broaden significantly with increasing nanotube diameter, making observations below 100 cm^{-1} difficult.[2,17] However, extremely narrow Raman lines (~0.35 cm^{-1}) in the RBM region have been measured for an inner tube of a double-wall nanotube (DWNT) (Refs. 18–21) and were attributed to the clean environment inside the outer nanotube. Even in the case of SWNTs, recent measurements by Rao *et al.*, using suspended SWNTs, have indicated that the minimum width of the RBM mode could be as small as ~0.7 cm^{-1}.[22,23]

Raman spectra of SWNTs in the 60–100 cm^{-1} frequency region have been investigated recently, but the spectral region below 60 cm^{-1}, where relatively weak $E_2(E_{2g})$ ring modes (RMs), $E_1(E_{1g})$ low-energy longitudinal optical modes (LELOMs), and large-diameter nanotube $A_1(A_{1g})$ RBMs are located,[1,24–26] has remained unexplored.

As has been demonstrated in earlier studies,[27–29] surface-enhanced Raman scattering (SERS) provides two important advantages for studying SWNTs, i.e., localization of the electromagnetic field to nanometer-scale regions and large enhancement factors. SERS also allows observation of very intense Raman forbidden modes due to symmetry breaking in the strong gradients of electric field near the metal surface.[30]

Using SERS Azoulay *et al.* have observed Raman lines that have been tentatively assigned to the low-energy modes, E_{1g} (LELOMs).[28,29] However, despite many interesting studies in this field,[27–29,31–35] the advantages of SERS for studying SWNTs have not been fully realized. SERS should allow the spectroscopic interrogation of highly localized (few nanometer) regions of a nanotube, permitting the observation of narrow resonances from clean, defect-free segments. However, because of the lack of a suitable SERS matrix and nanotube samples, such narrow resonances have not been seen until now.

Here we report the discovery of very narrow Raman lines in the low-frequency region (10–100 cm^{-1}) of the SERS spectra of SWNTs. In this work, suspended and randomly oriented SWNTs at the top of vertically aligned carbon nanotube arrays (VANTAs) were used for SERS studies. Gold deposited onto the disordered layer at the top of VANTAs created extremely intense SERS "hot spots" which resulted in very narrow individual resonances, pairs of resonances with identical excitation profiles, and previously unobserved resonances with very low frequencies. The narrow and intense SERS lines are thought to occur from the high degree of field localization on "clean," defect-free regions of individual SWNTs.

II. EXPERIMENTAL

VANTAs with a layer of low-density, randomly-oriented SWNTs at the top were grown by chemical vapor deposition (CVD). The CVD growth procedure of VANTAs has been described in detail in Ref. 36. Briefly, the VANTAs were grown at 750 °C in flowing Ar/H_2 from preannealed Mo (0.5 nm)/Fe (1 nm) catalyst films deposited on a Si substrate covered with a 10 nm Al buffer layer. These conditions resulted in the growth of relatively long arrays [Figs. 1(a)–1(c)] with a disordered layer of free-standing SWNTs at the top, depicted in Fig. 1(a). This disordered layer [Fig. 1(c)] arises from the first nanotubes, which nucleate and grow. As nanotubes grow from nanoparticles anchored to the substrate, this layer is pushed up when the density of the nanotubes forces the vertical alignment and coordinated

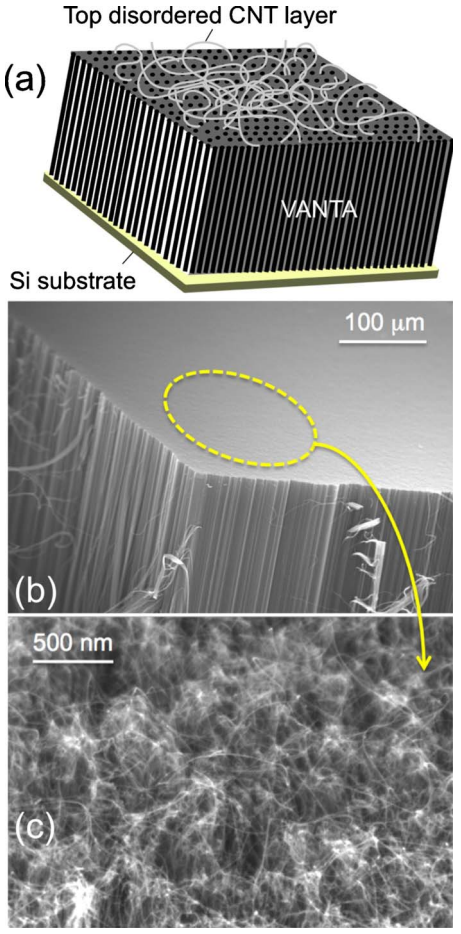

FIG. 1. (Color online) (a) Schematic of a VANTA, (b) SEM images of a pristine carbon nanotube array, and (c) its top disordered layer.

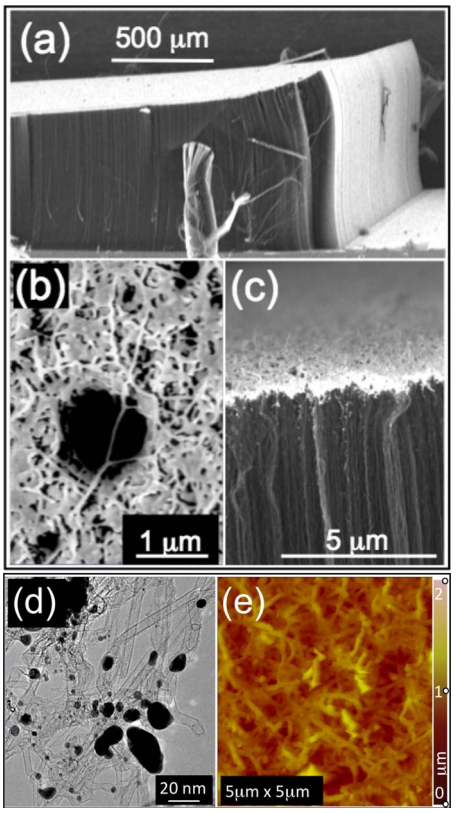

FIG. 2. (Color online) [(a)–(c)] SEM images of VANTAs with a gold layer at the top; [(a) and (c)] side on view, (b) top view. (d) A TEM image of VANTAs after decoration with gold showing SWNTs and gold nanoparticles. (e) An AFM image of the top layer of the VANTA decorated with gold.

growth of the array. The attractive feature of the VANTA samples for Raman studies is the wide variety of free-standing SWNTs having a broad distribution of diameters (1–5 nm).

To fabricate a SERS matrix, a gold layer was deposited on top of these arrays using electron-beam deposition. Figures 2(a)–2(c) show scanning electron microscopy (SEM) images of VANTAs with a gold layer at the top. These images show that the web morphology of the top nanotube layer is still preserved after gold deposition, even though almost all the nanotubes were covered with gold. The average thickness of the gold layer around the nanotubes is about 20 nm. These nanotubes also were characterized using transmission electron microscopy (TEM) and atomic force microscopy (AFM) [Figs. 2(d) and 2(e)]. TEM confirmed the presence of SWNTs with a broad diameter distribution while AFM showed the morphology of the top layer coated with gold.

Raman spectra were acquired at room temperature using a confocal, tunable micro/macro-Raman system (Jobin Yvon Horiba, T64000) based on a triple monochromator. A tunable, cw-Ti:sapphire laser (685–1000 nm, 6 GHz linewidth, Coherent Mira 900) was used to measure Raman excitation resonances in the 685–800 nm spectral region. To suppress the fluorescence background of the laser, the beam was passed through a small monochromator (MicroHR, Horiba Jobin Yvon, 1200 grooves/mm holographic grating). In cases where a HeNe laser (632.8 nm, 35 mW, Coherent) was used as an excitation source, two 1 nm band-pass interference filters were used to remove the fluorescence background. The scattered light was collected through a microscope in backscattering configuration using a long working distance microscope objective (100×, NA=0.8). The laser power at the sample was varied from 3 μW to 1 mW with a spot size of $\sim$1 μm, and typically several "hot spots" were found within a 50×50 μm^2 area. Typical acquisition times were only 10–20 s. The intensities of Raman lines acquired at each excitation wavelength were corrected for the instrument response and ν^4 factor. Frequency calibration was performed using a Ne calibration lamp, the spectral lines of which were fitted with a Gaussian profile to determine the instrument's spectral resolution [$\sim$0.7 cm^{-1} full width at half maximum (FWHM)].

III. RESULTS AND DISCUSSION

A. Individual SERS resonances

20 individual SERS resonances and their excitation profiles in Stokes (S) and anti-Stokes (AS) regions were measured and assigned to specific SWNTs (Table I). Figure 3(a) presents an example. While the majority of these lines were

TABLE I. Experimental frequencies (ω_{exp}), measured and deconvoluted (γ_m, γ_d) linewidths (FWHM), experimental optical transition energies and linewidths $\{E_{ii}^{exp}, \Gamma(\text{FWHM})\}$, calculated transition energies (E_{ii}^{calc}), nanotube indices (n,m), and diameter (d).

ω_{exp} (cm^{-1})	γ_m (cm^{-1})	γ_d (cm^{-1})	E_{ii}^{exp} (eV)	Γ (meV)	E_{ii}^{calc} (eV)	(n,m) branch	d (nm)
308.3	1.3	1.0	1.651	45	1.852	(9,1) S22L	0.747
262.3	1.9	1.7	1.744	46	1.722	(10,2) S22L	0.872
232.4	1.3	1.0	1.627	45	1.601	(11,3) S22L	1.000
222.6	1.9	1.7	1.649	75	1.614	(10,5) S22L	1.036
222.0	1.5	1.3	1.658	61	1.614	(10,5) S22L	1.036
204.2	2.6	2.5	1.689	45	1.699	(14,1) S22H	1.137
203.2	2.3	2.1	1.685	37	1.699	(14,1) S22H	1.137
199.8	2.5	2.4	1.653	65	1.667	(13,3) S22H	1.153
193.3	1.1	0.8	1.619	62	1.608	(12,5) S22H	1.185
185.1	3.0	2.9	1.713	52	1.854	(16,1) M11L	1.294
169.4	0.84	0.3	1.739	36	1.749	(18,0) M11L	1.409
					1.747	(17,2)	1.416
158.9	1.1	0.8	1.678	45	1.711	(14,8) M11L	1.510
147.3	1.8	1.6	1.660	46	1.651	(12,12) M11L	1.627
105.7	1.3	1.1	1.718	80	1.724	(21,10) S33L	2.146
104.4	1.0	0.5	1.683	80	1.680	(27,1) S33L	2.154
					1.679	(26,3)	2.163
					1.676	(25,5)	2.180
					1.670	(24,7)	2.205
100.2	1.2	0.9	1.699	55	1.693	(19,14) S33L	2.246
					1.693	(19,15) S33H	2.311
100.1	0.84	0.3	1.784	75	1.769	(24,8) S33H	2.258
						(25,6) S33H	2.230
83.6	2.2	2.1	1.651	50	1.693	(35,0) S44L	2.740
					1.693	(34,2)	2.744
					1.690	(33,4)	2.754
					1.685	(32,6)	2.770
72.5	1.5	1.3	1.749	67	1.767	(34,10) M22L	3.128
69.4	1.4	1.2	1.688	20	1.691	(42,0) M22L	3.288
					1.691	(41,2)	3.291
					1.689	(40,4)	3.299

accurately fit by a Voigt profile, an interesting feature of this particular spectrum is the clear asymmetry of the line shape that slightly deviates from the fit. The deconvoluted linewidth of this line, tentatively assigned to the (14,8) nanotube, is estimated to be ~ 0.8 cm^{-1} (FWHM). In general, the deconvoluted linewidths (FWHM) of these resonances varied from 0.3 to 2.9 cm^{-1} (Table I). These variations may arise from differences in the broadening induced by the presence of defects and/or contaminants in the probed regions on each SWNT. Another possible explanation is large variations in the anharmonic broadening of the RBMs depending on nanotube chirality.[22,23]

The corresponding Raman excitation profiles for the Stokes and anti-Stokes lines were fit with the function $I_{S,AS}(E_{ii},\Gamma)$ (Ref. 9) [see caption to Figs. 3(a)–3(c)] to determine the energy, E_{ii}, and the width, Γ (FWHM), of the corresponding optical transition [Fig. 3(b)]. In the case when $\Gamma \geqslant \hbar\omega$, two resonances—the first one with the excitation laser $E_{ii}=E_{las}$ and the second one with the Stokes (or anti-Stokes) scattered light $E_{ii}=E_{las} \mp \hbar\omega$—overlap, giving only one excitation profile for each Stokes and anti-Stokes Raman lines, that are centered at $\pm\hbar\omega/2$, respectively, relative to the transition energy, E_{ii}, with a spacing of $\hbar\omega$. This is different from the case when the width of the resonance, Γ (FWHM), is smaller than the corresponding phonon energy, $\hbar\omega$ ($\Gamma < \hbar\omega$) when the spacing between the Stokes and anti-Stokes excitation profiles is $2\hbar\omega$.

The excitation power dependences of the Stokes and anti-Stokes SERS lines ($\omega=222.0$ cm^{-1}) were measured for laser energies between 20 and 900 μW. As shown in Fig. 3(c), in all cases a linear region is observed at lower laser powers, which is followed by a marked decrease in slope. The exact

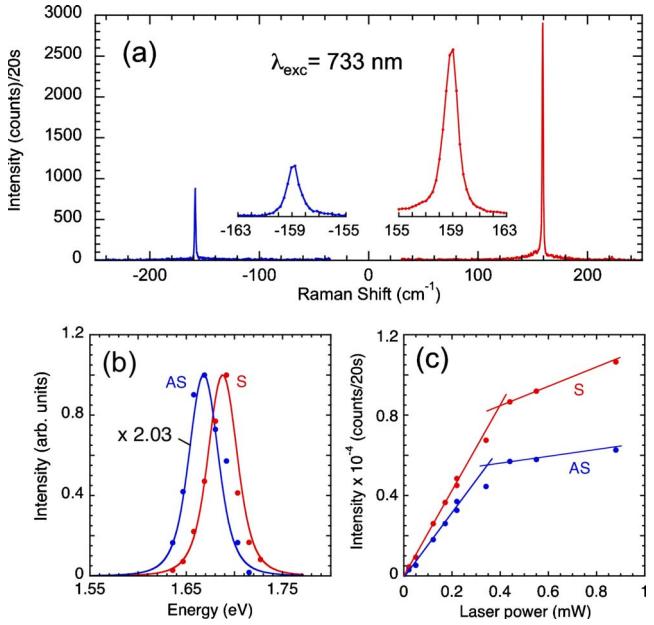

FIG. 3. (Color online) (a) Stokes (S) and anti-Stokes (AS) SERS spectra showing single narrow peaks at $\omega=158.9$ cm^{-1}. Insets show the magnified view of the same peaks. The incident laser power was 0.22 mW. (b) Experimental Stokes and anti-Stokes Raman excitation profiles (dots) measured with 5 nm increments using a tunable Ti:sapphire laser. The anti-Stokes intensity is scaled up by a factor of 2.03. The solid lines show fits to these profiles using the following function (Ref. 9): $I_{S,AS}(E_{ii},\Gamma)=\frac{A}{(\hbar\omega)^2}\left|\frac{1}{E_{las}-E_{ii}-i\Gamma/2}-\frac{1}{E_{las}\mp\hbar\omega-E_{ii}-i\Gamma/2}\right|^2$, where A is a constant, ω is the frequency of the Raman line, E_{las} is the excitation energy, and E_{ii} and Γ (adjustable fit parameters) are the energy and the width (FWHM) of the corresponding electron transition. (c) Intensities of the Stokes and anti-Stokes SERS lines versus laser power ($\omega=222.0$ cm^{-1}).

laser power where this deviation occurs varied for each hot spot. This dependence was reversible and reproducible. However, when the laser power exceeded a few milliwatts, the intensity of the SERS lines dropped irreversibly (not shown), which is likely due to a thermally induced change in the nanoparticle-nanotube configuration where the high-field enhancement occurs.

Assignment of the observed SERS lines was based on the approach employed in Refs. 12, 14, and 15 for as-produced vertically aligned arrays of SWNTs having a broad diameter distribution. We applied this procedure to assign the Raman spectra of our pristine VANTAs (before gold deposition) acquired using a HeNe laser (633 nm, 1.96 eV) [Figs. 4(a)–4(c)] and a tunable Ti:sapphire laser (694–739 nm, 1.79–1.68 eV) (not shown). It was found that the relationship, $\omega_{RBM}=227.0/d$,[14] and the other parameters from Refs. 12 and 15 (see caption to Fig. 5), that describe the transition energies, $E_{ii}(n,m)$, for different nanotubes, give good agreement between the measured and calculated spectra for pristine VANTAs [Figs. 4(a)–4(c)]. The Raman spectra of pristine VANTAs measured at 633 nm show many relatively strong overlapping lines in the spectral range from 70 to 230 cm^{-1}. We did not observe any strong Raman lines in the low-frequency region, below 70 cm^{-1} even with a relatively large acquisition time (5 min) used to measure the spectra.

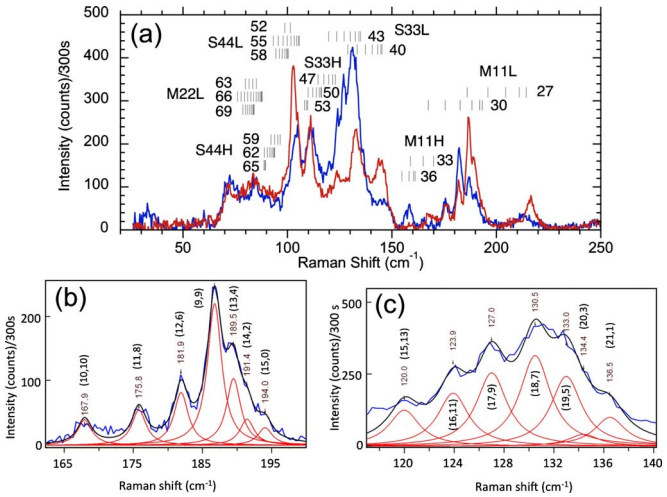

FIG. 4. (Color online) (a) Raman spectra of pristine VANTAs (Fig. 1) measured before gold deposition and acquired from the top of the array using an excitation wavelength of 633 nm (1.96 eV). The two traces correspond to different spots on the array. The vertical lines show the theoretical frequencies of the nanotubes in the range of transition energies of 1.96 ± 0.05 eV using $\omega=227.0/d$, where d is the nanotube diameter. The peaks in the spectral regions of (b) 165–200 cm^{-1} and (c) 100–140 cm^{-1} were fitted with Lorentzians [(b) 2.5 cm^{-1} FWHM and (c) 3.0 cm^{-1} FWHM] and the corresponding maximum frequencies are listed in the figures together with the nanotube indices (n,m) assigned according to the procedure outlined in the caption to Fig. 5. The numbers in (a) mark the corresponding $2n+m$ branches (low, L, and high, H) for metallic (M) and semiconducting (S) nanotubes.

As a first approximation we used the same procedure to interpret the SERS spectra of gold-decorated nanotubes. The tentative identification of the 120 SERS lines acquired using a HeNe laser in the energy range of 1.96 ± 0.05 eV was performed in the spectral range of 50–300 cm^{-1}. We found that for the E_{22}^{S} transition, only a relatively small up-shift of a few wavenumbers was required to match the experimental ω_{RBM}. For the E_{11}^{M} transition, however, a larger up-shift of 7.5 cm^{-1} was necessary to match the experimental lines. Although it is difficult to perform assignment of the larger diameter nanotubes corresponding to E_{33}^{S}, E_{44}^{S}, E_{22}^{M} transitions, we found that the observed ω_{RBM} pattern and the calculated one were well matched without any apparent shift.

Figure 5 shows the experimental transition energies obtained by fitting the measured Raman excitation profiles for every observed ω_{RBM} (Table I) and their comparison with the calculated $E_{ii}(n,m)$ that are up-shifted in ω_{RBM} by 3 cm^{-1} and 7.5 cm^{-1} for the E_{22}^{S} and E_{11}^{M}, respectively. The majority of the measured transition energies match the calculated ones with only slight deviations that depend on the particular branch of the corresponding E_{ii}. For example, the experimental points assigned to the (10, 2), (11, 3), and (10, 5) nanotubes from the lower branch of E_{22}^{SL} (S22L) deviate from the calculated transition energies by 20–40 meV while the points corresponding to the (14, 1), (13, 3), and (12, 5) tubes from the upper branch of the same transition (S22H) have smaller deviations of −10 meV, −14 meV, and 11 meV, respectively (Table I). However, two measured SERS lines at 308.3 and

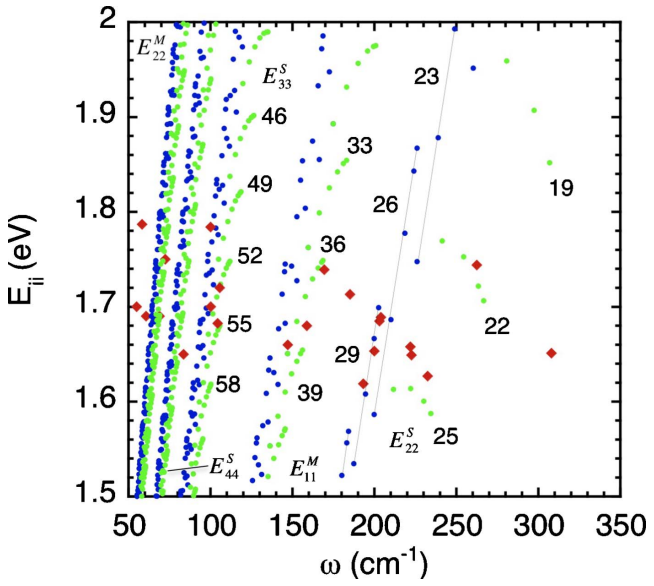

FIG. 5. (Color online) Optical transition energies (dots) as a function of RBM frequency calculated using the equations from Refs. 12 and 15. $E_{ii}(n,m)=(\beta_p \cos 3\theta)/d^2+a_d^p(1+b\log\frac{c}{p/d})+\binom{0}{0.0596p/d}^{\text{for } E_{11}^S,E_{22}^S,E_{11}^M}_{\text{for } E_{33}^S,E_{44}^S,E_{22}^M}$, where $\theta=\arctan(\frac{n\sqrt{3}}{2n+m})$, $d=0.142\sqrt{3(n^2+nm+m^2)}/\pi$, $a=1.074$ eV nm, $b=0.467$ nm^{-1}, and $c=0.812$ nm^{-1} and the parameters β_p, p for each branch of the corresponding optical transitions are as follows: $E_{11}^{SL}(-0.07,1)$; $E_{11}^{SH}(0.05,1)$; $E_{22}^{SL}(-0.9,2)$; $E_{22}^{SH}(0.14,2)$; $E_{11}^{ML}(-0.18,3)$; $E_{11}^{MH}(0.29,3)$; $E_{33}^{SL}(-0.42,4)$; $E_{33}^{SH}(0.42,4)$; $E_{44}^{SL}(-0.4,5)$; $E_{44}^{SH}(0.4,5)$; $E_{22}^{ML}(-0.6,6)$; $E_{22}^{MH}(0.57,6)$, and $\omega_{RBM}=(227.0/d)+C$, where d is nanotube diameter and $C=(3,7.5,0,0,0)\pm1$ cm^{-1} for E_{22}^S, E_{11}^M, E_{33}^S, E_{44}^S, and E_{22}^M, respectively. The diamonds show the experimental transition energies obtained by fitting the measured Raman excitation profiles for every SERS line [see Fig. 3(b) and Table I]. The numbers mark the corresponding $2n+m$ branches.

185.1 cm^{-1} are shifted considerably from their calculated E_{ii} by −201 and −141 meV, and can be explained by a possible bundling effect which lowers the transition energies. The shifts of the ω_{RBM} and the corresponding transition energies for different transitions are typical for SWNTs in different environments, e.g., in different surfactants, and have been studied before.[9] This interaction depends on nanotube diameters and chiralities, and the type of an environment. We found that similar behavior occurs for SWNTs interacting with gold nanostructures, although the larger diameter tubes seem to exhibit much smaller deviations from the calculated ω_{RBM} and $E_{ii}(n,m)$. The gold layer can also modify the screening of the electron-hole interaction that results in changes in the electronic energy transitions.[37]

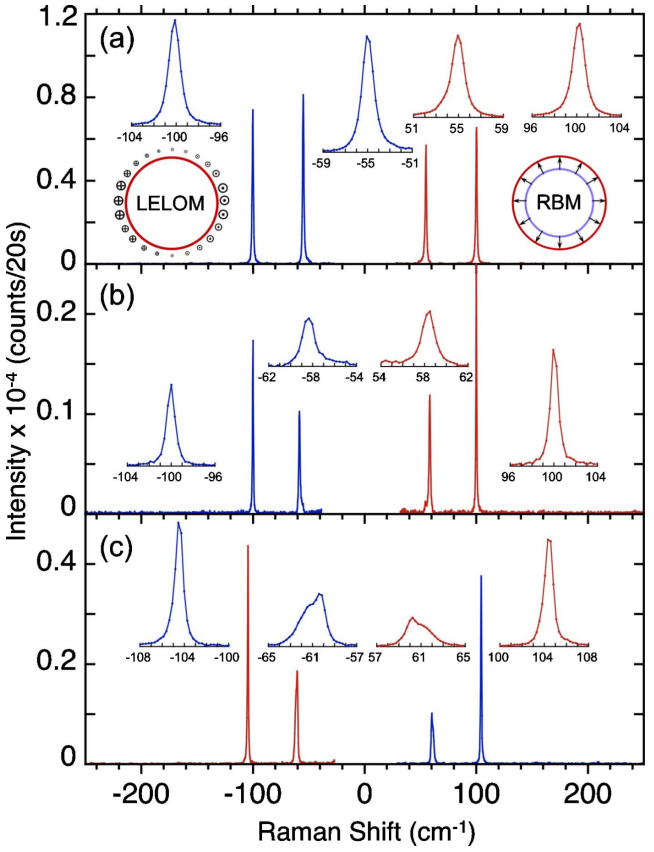

FIG. 6. (Color online) Stokes and anti-Stokes SERS spectra showing pairs of narrow lines at (a) $\omega_1/\omega_2=55.0/100.2$ cm^{-1}, $\lambda_{exc}=733$ nm, (b) 58.3 cm^{-1}/100.1 cm^{-1}, $\lambda_{exc}=689$ nm, and (c) 60.8/104.4 cm^{-1}, $\lambda_{exc}=733$ nm. The incident laser power was 0.22 mW. Insets show the magnified view of the same peaks and the displacement patterns of LELOMs and RBMs in (a). The symbols, ⊕ and ⊙, indicate downward and upward arrows parallel to the nanotube axis with the diameter of the symbols proportional to the arrow length.

TABLE II. Experimental ω_{exp} and calculated ω_{LELOM} (1) and ω_{LELOM} (2) frequencies, measured γ_m and deconvoluted γ_d linewidths (FWHM), optical transition energy E_{ii} and linewidths (FWHM), Γ of the corresponding excitation profiles for the observed pairs of SERS lines.

Mode	ω_{exp} (cm^{-1})	$\omega_{LELOM}(1)$ (cm^{-1})	$\omega_{LELOM}(2)$ (cm^{-1})	γ_m (cm^{-1})	γ_d (cm^{-1})	E_{ii}^{exp} (eV)	Γ (meV)
RBM	104.4			1.0	0.5	1.683	80
LELOM	60.8	60.0	68.2	1.4	1.2		
RBM	100.2			1.2	0.9	1.699	55
LELOM	55.0	57.3	65.5	1.3	1.1		
RBM	100.1			0.84	0.3	1.784	75
LELOM	58.3	57.3	65.4	1.4	1.2		

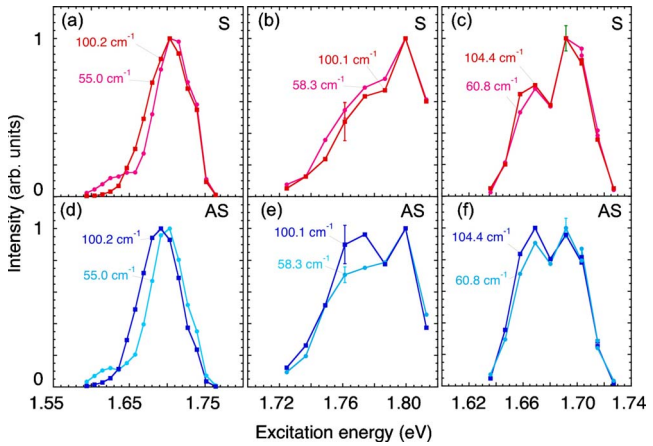

FIG. 7. (Color online) Experimental Stokes (S) and anti-Stokes (AS) Raman excitation profiles measured with 5 nm increments for the [(a) and (d)] ω_1/ω_2=55.0/100.2 cm^{-1}, [(b) and (e)] 58.3/100.1 cm^{-1}, and [(c) and (f)] 60.8/104.4 cm^{-1} pairs, respectively. The incident laser power in all cases is 0.22 mW. The profiles are normalized to their maxima. The measured I_{AS}/I_S ratios at the maxima were: 1.2 ± 0.3 and 1.0 ± 0.3 for the 55.0 cm^{-1} and 100.2 cm^{-1} lines; 0.7 ± 0.2 for both 58.3 cm^{-1} and 100.1 cm^{-1} lines; and 1.7 ± 0.3 and 1.1 ± 0.3 for the 60.8 cm^{-1} and 104.4 cm^{-1} lines, respectively.

B. Pairs of SERS resonances

In several cases we observed pairs of narrow lines at ω_1 and ω_2 in the SERS spectra that exhibited very similar Raman excitation profiles and laser power dependences. The Stokes and anti-Stokes SERS spectra of three different pairs are shown in Figs. 6(a)–6(c). The corresponding frequencies, the optical transition energies, and the linewidths (FWHM) of the three different pairs measured at the incident laser energy of 0.22 mW are listed in Table II. The linewidths decreased when the incident power dropped from 0.22 to 0.003 mW. For example, for the ω_1/ω_2=55.0/100.2 cm^{-1} pair [Fig. 6(a)] the deconvoluted linewidths, γ_d, of both resonances decreased from 1.0 ± 0.1 to 0.7 ± 0.1 cm^{-1}. The frequencies of these lines were downshifted linearly from 55.1 to 55.0 ± 0.05 cm^{-1} and from 100.6 to 100.2 ± 0.05 cm^{-1} when the incident energy increased from 0.003 to 0.22 mW. This behavior is consistent with the inherent anharmonicity of the corresponding modes. In some cases we observed splitting of the low-frequency component. For example, the low-frequency line of the 60.8/104.4 cm^{-1} pair is split into two components, which are separated by $\sim$1 cm^{-1} [Fig. 6(c), insets].

The corresponding excitation profiles of the three pairs (ω_1/ω_2=55.0/100.2 cm^{-1}, 58.3/100.1 cm^{-1}, and 60.8/104.4 cm^{-1}) are shown in Figs. 7(a)–7(f). For each SERS line, the Raman excitation profiles are nearly identical in the Stokes and anti-Stokes regions, as expected. The excitation profiles for both lines in each pair also are very similar to one another, including asymmetry. For example, for the 55.0/100.2 cm^{-1} pair of Figs. 7(a) and 7(d), both profiles are asymmetric and only the low-energy side shows a pronounced feature for the 55.0 cm^{-1} line. The other two pairs also show remarkable similarity in their excitation profiles for the ω_1 and ω_2 SERS lines [see Figs. 7(b), 7(c), 7(e), and 7(f)].

Moreover, the dependence of the peak Stokes and anti-Stokes intensities for each line follows the same response on laser power between 0.003 and 0.22 mW, as shown in Figs. 8(a) and 8(d) for the 55.0/100.2 cm^{-1}, Figs. 8(b) and 8(e) for the 58.3/100.1 cm^{-1}, and Figs. 8(c) and 8(f) for the 60.8/104.4 cm^{-1} pairs.

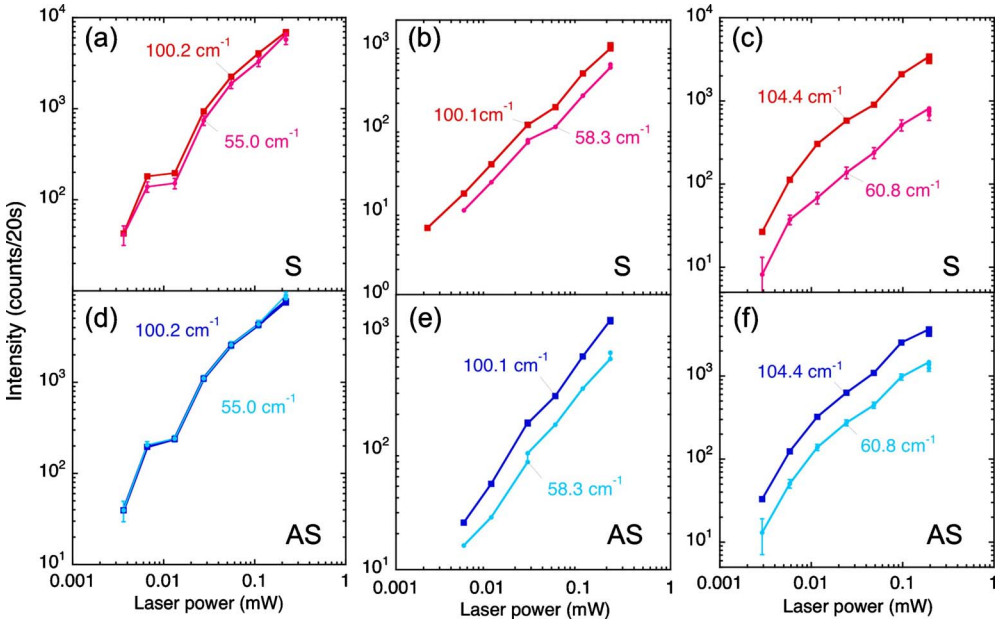

FIG. 8. (Color online) Peak intensities of Stokes (S) and anti-Stokes (AS) Raman lines versus laser power: [(a) and (d)] ω_1/ω_2 =55.0/100.2 cm^{-1} (λ_{exc}=733 nm), [(b) and (e)] 58.3/100.1 cm^{-1} (λ_{exc}=704 nm), and [(c) and (f)] 60.8 cm^{-1}/104.4 cm^{-1} (λ_{exc} =733 nm). The extra point in each case at the highest laser power (0.22 mW) was measured at the end of the experiment to verify stable behavior of the corresponding hot spot during the measurements.

One explanation for the observed pairs of resonances is that they originate from RBMs of individual DWNTs. However, using the observed ω_1 and ω_2 as candidate radial breathing-like modes of DWNTs, current existing theories predict incompatible combinations of SWNT diameters.[38,39] Another possibility is a bundle of two nanotubes coupled by van der Waals interaction. As it has been demonstrated by Débarre *et al.*,[40] the RBM of a larger diameter nanotube can be mechanically coupled with a specific resonant harmonic of a ring mode from a smaller diameter SWNT, resulting in sufficiently efficient electronic coupling between the nanotubes to produce similar Raman excitation profiles for both RBM lines. However, in our case this theory cannot explain the observed spitting of the lower frequency SERS line in the case of the 60.8 cm^{-1} line [Fig. 6(c)].

A better explanation is that both lines, ω_1 and ω_2, originate from the same region of an individual SWNT and simply belong to different modes of the same nanotube. It has been well established theoretically[1,24–26] that in addition to the radial breathing mode (RBM), there are other Raman active low-energy modes, i.e., LELOMs and RMs. The frequencies of these modes have been calculated using continuum and force-constant models, and simple analytical equations have been derived.[25,26] According to Ref. 26 the frequencies, ω_{RM} and ω_{LELOM}, of these modes relative to the ω_{RBM} are

$$\omega_{RM}(\lambda) = \omega^0_{RM}\frac{\omega^2_{RBM}}{(\omega^0_{RBM})^2}(\lambda^2 - 1),$$

$$\omega_{LELOM}(\lambda') = \frac{\omega^0_{LELOM}}{\omega^0_{RBM}}\omega_{RBM}\lambda', \quad (1)$$

where $\omega^0_{RBM}=486$ cm^{-1}, $\omega^0_{RM}=54$ cm^{-1}, $\omega^0_{LELOM}=278$ cm^{-1}, and λ, λ' are integers that select certain ring and low-energy longitudinal optical modes, respectively. The continuum model based on oscillations of a thin hollow cylinder predicts[25]

$$\omega_{RM}(\lambda) = \frac{\alpha}{\sqrt{3}}\frac{\lambda(\lambda^2-1)}{\sqrt{\lambda^2+1}}\omega_{RBM}, \quad \omega_{LELOM}(\lambda') = \frac{\omega_{RBM}\lambda'}{2\sqrt{1-r}}, \quad (2)$$

where the parameters α and r are estimated as 0.086 and 0.415, respectively. The values of the $\omega_{LELOM}(\lambda'=1)$ calculated using Eqs. (1) and (2) are listed in Table II. The estimate of the ω_{LELOM} based on Eq. (1) agrees well with the experimental values of ω_1 and only slightly deviates from the experimental ω_1 [$\omega_{LELOM}(1)-\omega_1=-0.8$, 2.3, and 1.0 cm^{-1} for the three ω_1 lines listed in Table II, respectively]. The continuum theory [Eq. (2)] gives the ω_{LELOM} that are upshifted by ~8 cm^{-1} compared to the experimental values.

The observed splitting of the 60.8 cm^{-1} line [Fig. 6(c)] is consistent with the degenerate character of $E_1(E_{1g})$ LELOMs. Since RBMs and LELOMs have different symmetries, $A_1(A_{1g})$ and $E_1(E_{1g})$, respectively, their relative intensities depend on the nanotube orientations relative to the laser beam.[24] Simultaneous observation of both RBM and LELOM is possible only for some orientations that in our experiment are randomly selected by choosing a specific hot spot.

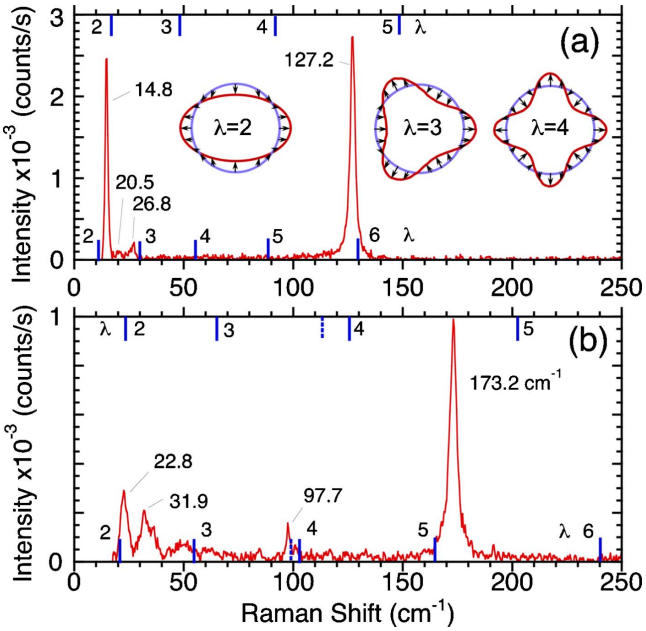

FIG. 9. (Color online) Low-frequency SERS peaks at (a) 14.8 cm^{-1} and (b) 22.8 and 31.9 cm^{-1}. The spectra were measured using a 633 nm HeNe laser (1.96 eV). The peak at 14.8 cm^{-1} was tentatively assigned to the low-energy ring mode of the (17, 9) nanotube with the corresponding RBM SERS line at 127.2 cm^{-1} ($E^S_{33}=1.97$ eV). The peaks at 22.8 cm^{-1} and 97.7 cm^{-1} were assigned to the RMs and the LELOMs, respectively. The corresponding RBM at 173.2 cm^{-1} was assigned to the (10,10) or (13,7) nanotubes with $E^M_{11}=1.89$ eV and 1.95 eV, respectively. The solid vertical lines at the top and the bottom correspond to the continuum (Ref. 25) and force-constant (Ref. 26) models, respectively. Insets show the displacement patterns for the ring mode for $\lambda=2-4$ (Ref. 26). The dashed vertical lines show the calculated positions of the LELOM for $\lambda'=1$ from the models (Ref. 25) (top) and Ref. 26 (bottom).

C. Low-frequency SERS resonances

In addition to higher frequency lines, Figs. 9(a) and 9(b) show very low-frequency SERS lines in the range of 14–30 cm^{-1}. Although the corresponding hot spots were not stable enough to permit the measurement of excitation profiles for these SERS lines, the relative frequencies between the different lines in each spectrum can still be examined using the theories from Refs. 25 and 26 to investigate whether these low-frequency resonances might be related to the RBM and RM of the same nanotube. The peak at 127.2 cm^{-1} [Fig. 4(a)] can be tentatively assigned to the RBM of the (17,9) nanotube with $E^S_{33}=1.97$ eV. Using the force-constant[26] and continuum[25] models, the ring mode $\omega_{RM}(\lambda=2)$ for this nanotube is predicted to be 11.1 cm^{-1} and 17.0 cm^{-1}, respectively, which agrees well with the measured value at 14.8 cm^{-1}. Similarly, ring and low-energy longitudinal optical modes predicted for the observed RBM in Fig. 9(b) agree with the calculated positions, as shown by

vertical lines. This match of the experimental data with theory based on the RM and LELOM supports our interpretation of the very low-frequency SERS lines, although measurements of the excitation profiles are necessary to get additional confirmation of this assignment. Additional low-frequency modes are observed (at 26.8 and 31.9 cm^{-1}) in Fig. 4 but could not be assigned at this time.

IV. CONCLUSIONS

Small regions of suspended SWNTs exposed by the evaporated Au layer are likely responsible for the hot spots which generate the intense Raman scattering and highly sharpened SWNT RBM features. This simple procedure to fabricate high numbers of SERS hot spots produces intense signals with a maximum observed SERS/Raman ratio of ~1900. The actual enhancement factors are much higher due to the large difference in the sizes of the SERS-active and Raman-active spatial regions.

Some SERS lines are almost ten times narrower than those measured and predicted theoretically for individual SWNTs. It is proposed that such narrow linewidths (as small as 0.3 cm^{-1}) might result from the structural perfection and cleanliness of the very short regions probed in this type of SERS matrix. This approach allows one to reveal true homogeneous anharmonic broadening of SERS lines, which opens new possibilities of using linewidths for chirality assignments.[23]

This unique SERS matrix created by gold decoration of loosely suspended SWNTs has enabled high-resolution spectroscopy of previously unexplored low-energy Raman modes of individual SWNTs. Such low-energy modes in 1D systems have been the subject of continuous theoretical studies during the past 10 years due to importance of these modes for the fundamental understanding of electron-phonon interactions that define the resistivity, magnetoresistance, and superconductivity in 1D systems.[41] Similar low-energy modes exist for nanotubes of any material as predicted by continuum models based upon a thin cylinder.[25] Like the RBM, the frequency of the low-energy $E_1(E_{1g})$ mode is inversely proportional to the tube diameter and can be used for SWNT diameter measurements. The technique should allow the diameter and chirality dependences of all nanotubes to be assigned with higher precision, enabling refinements in the fitting parameters of current theories. This type of SERS matrix enabled the observation of RBMs for SWNTs with diameters above 3 nm, opening the door for the metrology of large diameter nanotubes which was not previously thought possible.[2]

High-resolution Raman spectroscopy of other nanotubes, nanowires, and single molecules should be enabled through the facile creation of numerous hot spots by the metal decoration of loosely suspended nanomaterials.

ACKNOWLEDGMENTS

This research was conducted at the Center for Nanophase Materials Sciences, which is sponsored at Oak Ridge National Laboratory by the Division of Scientific User Facilities, U.S. Department of Energy. Materials synthesized under research sponsored by the Materials Sciences and Engineering Division, Office of Basic Energy Sciences, U.S. Department of Energy.

[1] A. M. Rao, E. Richter, S. Bandow, B. Chase, P. C. Eklund, K. A. Williams, S. Fang, K. R. Subbaswamy, M. Menon, A. Thess, R. E. Smalley, G. Dresselhaus, and M. S. Dresselhaus, Science **275**, 187 (1997).

[2] M. S. Dresselhaus, G. Dresselhaus, and A. Jorio, J. Phys. Chem. C **111**, 17887 (2007).

[3] M. S. Dresselhaus, G. Dresselhaus, and M. Hofmann, Vib. Spectrosc. **45**, 71 (2007).

[4] A. G. Souza Filho, A. Jorio, J. H. Hafner, C. M. Lieber, R. Saito, M. A. Pimenta, G. Dresselhaus, and M. S. Dresselhaus, Phys. Rev. B **63**, 241404(R) (2001).

[5] M. S. Strano, S. K. Doorn, E. H. Haroz, C. Kittrell, R. H. Hauge, and R. E. Smalley, Nano Lett. **3**, 1091 (2003).

[6] G. G. Samsonidze, R. Saito, N. Kobayashi, A. Gruneis, J. Jiang, A. Jorio, S. G. Chou, G. Dresselhaus, and M. S. Dresselhaus, Appl. Phys. Lett. **85**, 5703 (2004).

[7] H. Telg, J. Maultzsch, S. Reich, F. Hennrich, and C. Thomsen, Phys. Rev. Lett. **93**, 177401 (2004).

[8] S. K. Doorn, D. A. Heller, P. W. Barone, M. L. Usrey, and M. S. Strano, Appl. Phys. A: Mater. Sci. Process. **78**, 1147 (2004).

[9] J. Maultzsch, H. Telg, S. Reich, and C. Thomsen, Phys. Rev. B **72**, 205438 (2005).

[10] S. K. Doorn, J. Nanosci. Nanotechnol. **5**, 1023 (2005).

[11] T. Michel, M. Paillet, J. C. Meyer, V. N. Popov, L. Henrard, and J. L. Sauvajol, Phys. Rev. B **75**, 155432 (2007).

[12] P. T. Araujo, S. K. Doorn, S. Kilina, S. Tretiak, E. Einarsson, S. Maruyama, H. Chacham, M. A. Pimenta, and A. Jorio, Phys. Rev. Lett. **98**, 067401 (2007).

[13] E. H. Haroz, S. M. Bachilo, R. B. Weisman, and S. K. Doorn, Phys. Rev. B **77**, 125405 (2008).

[14] P. T. Araujo, I. O. Maciel, P. B. C. Pesce, M. A. Pimenta, S. K. Doorn, H. Qian, A. Hartschuh, M. Steiner, L. Grigorian, K. Hata, and A. Jorio, Phys. Rev. B **77**, 241403(R) (2008).

[15] S. K. Doorn, P. T. Araujo, K. Hata, and A. Jorio, Phys. Rev. B **78**, 165408 (2008).

[16] M. S. Dresselhaus, G. Dresselhaus, R. Saito, and A. Jorio, Annu. Rev. Phys. Chem. **58**, 719 (2007).

[17] A. Jorio, C. Fantini, M. S. S. Dantas, M. A. Pimenta, A. G. Souza Filho, G. G. Samsonidze, V. W. Brar, G. Dresselhaus, M. S. Dresselhaus, A. K. Swan, M. S. Unlu, B. Goldberg, and R. Saito, Phys. Rev. B **66**, 115411 (2002).

[18] R. Pfeiffer, H. Kuzmany, C. Kramberger, C. Schaman, T. Pichler, H. Kataura, Y. Achiba, J. Kurti, and V. Zolyomi, Phys. Rev. Lett. **90**, 225501 (2003).

[19] R. Pfeiffer, C. Kramberger, F. Simon, H. Kuzmany, V. N. Popov, and H. Kataura, Eur. Phys. J. B **42**, 345 (2004).

[20] R. Pfeiffer, F. Simon, H. Kuzmany, and V. N. Popov, Phys. Rev. B **72**, 161404(R) (2005).

[21] H. Kuzmany, W. Plank, R. Pfeiffer, and F. Simon, J. Raman Spectrosc. **39**, 134 (2008).
[22] R. Rao, J. Menendez, C. D. Poweleit, and A. M. Rao, Phys. Rev. Lett. **99**, 047403 (2007).
[23] N. Bonini, R. Rao, A. M. Rao, N. Marzari, and J. Menendez, Phys. Status Solidi **245**, 2149 (2008).
[24] R. Saito, T. Takeya, T. Kimura, G. Dresselhaus, and M. S. Dresselhaus, Phys. Rev. B **57**, 4145 (1998).
[25] G. D. Mahan, Phys. Rev. B **65**, 235402 (2002).
[26] D. Gunlycke, H. M. Lawler, and C. T. White, Phys. Rev. B **77**, 014303 (2008).
[27] G. S. Duesberg, W. J. Blau, H. J. Byrne, J. Muster, M. Burghard, and S. Roth, Chem. Phys. Lett. **310**, 8 (1999).
[28] J. Azoulay, A. Débarre, A. Richard, P. Tchénio, S. Bandow, and S. Iijima, Chem. Phys. Lett. **331**, 347 (2000).
[29] J. Azoulay, A. Débarre, A. Richard, P. Tchénio, S. Bandow, and S. Iijima, Europhys. Lett. **53**, 407 (2001).
[30] M. Moskovits, D. P. DiLella, and K. J. Maynard, Langmuir **4**, 67 (1988).
[31] K. Kneipp, H. Kneipp, P. Corio, S. D. M. Brown, K. Shafer, J. Motz, L. T. Perelman, E. B. Hanlon, A. Marucci, G. Dresselhaus, and M. S. Dresselhaus, Phys. Rev. Lett. **84**, 3470 (2000).
[32] P. Corio, S. D. M. Brown, A. Marucci, M. A. Pimenta, K. Kneipp, G. Dresselhaus, and M. S. Dresselhaus, Phys. Rev. B **61**, 13202 (2000).
[33] T. Assmus, K. Balasubramanian, M. Burghard, K. Kern, M. Scolari, N. Fu, A. Myalitsin, and A. Mews, Appl. Phys. Lett. **90**, 173109 (2007).
[34] R. Kumar, H. Zhou, and S. B. Cronin, Appl. Phys. Lett. **91**, 223105 (2007).
[35] L. M. Tong, Z. P. Li, T. Zhu, H. X. Xu, and Z. F. Liu, J. Phys. Chem. C **112**, 7119 (2008).
[36] A. A. Puretzky, D. B. Geohegan, S. Jesse, I. N. Ivanov, and G. Eres, Appl. Phys. A: Mater. Sci. Process. **81**, 223 (2005).
[37] H. Lin, J. Lagoute, V. Repain, C. Chacon, Y. Girard, J.-S. Lauret, F. Ducastelle, A. Loiseau, and S. Rousset, Nature Mater. **9**, 235 (2010).
[38] E. Dobardžić, J. Maultzsch, I. Milošević, C. Thomsen, and M. Damnjanović, Phys. Status Solidi B **237**, R7 (2003).
[39] V. N. Popov and L. Henrard, Phys. Rev. B **65**, 235415 (2002).
[40] A. Débarre, M. Kobylko, A. M. Bonnot, A. Richard, V. N. Popov, L. Henrard, and M. Kociak, Phys. Rev. Lett. **101**, 197403 (2008).
[41] H. Suzuura and T. Ando, Phys. Rev. B **65**, 235412 (2002).